

D_3^+ and H_3^+ in intense laser fields studied with a quasiclassical modelErik Lötstedt,^{*} Tsuyoshi Kato, and Kaoru Yamanouchi*Department of Chemistry, School of Science, The University of Tokyo, 7-3-1 Hongo, Bunkyo-ku, Tokyo 113-0033, Japan*

(Received 6 February 2012; revised manuscript received 22 March 2012; published 8 May 2012)

The response of the D_3^+ and H_3^+ molecules to an intense, ultrashort laser pulse is investigated with a quasiclassical model to provide details of our previous short report [Phys. Rev. Lett. **106**, 203001 (2011)]. The stable, lowest-energy configuration of two electrons and three deuterons (or three protons) is realized by certain auxiliary, momentum-dependent potentials. The time evolution of the molecule in the external driving field leading to the dissociation and ionization is calculated by numerically solving the classical Hamiltonian equations of motion. It is shown that the theoretical results reproduce qualitatively characteristic features of the experimental angular distributions and kinetic energy release spectra [Phys. Rev. Lett. **103**, 103004 (2009)].

DOI: [10.1103/PhysRevA.85.053410](https://doi.org/10.1103/PhysRevA.85.053410)

PACS number(s): 33.80.Eh, 33.80.Wz, 34.10.+x, 02.70.Ns

I. INTRODUCTION

In molecular physics with lasers, the task is to investigate a complex interplay caused by two forces: the Coulombic force, acting between the constituting particles, and the electric force of the externally applied laser field. It is prerequisite to understand fully the correlated motion of laser-driven electrons and nuclei for achieving the ultimate goal of controlling molecular dynamics with the laser field [1]. On the experimental side, a variety of ingenious techniques have been developed to obtain detailed information of laser-induced molecular dynamics, both in small molecules such as diatomic H_2^+ [2–4], H_2 [5,6], triatomic H_3^+ [7–9], and in larger hydrocarbon molecules [10–13].

The challenge for theory is to include both the electronic and protonic degrees of freedom, which are necessary to model an experiment where both ionization and dissociation occur. If the nuclei are kept fixed, the quantum dynamics of the electrons may be solved exactly provided that not more than two electrons are involved [14,15]. For atomic and molecular systems having more than two electrons, only the highest occupied molecular orbital is taken into account in most cases [16–18]. On the other hand, one-electron systems may be solved also with nuclear motion included [19–23]. Other approaches which have been developed are mixed quantum-classical models treating the nuclei as classical particles and the electrons quantum mechanically [24–30], and fully quantum mechanical Monte Carlo wave-packet techniques, where the ionization step is treated only approximately [31,32]. We also note that approximate methods for aiming to treat quantum mechanically both electrons and nuclei in a molecule in a laser field have been developed [33–35], but their implementation for polyatomic molecules seems too demanding.

While we have no doubts that the quantum mechanical problem of such field-driven, polyatomic molecules will eventually be solved, the present status is that a complete quantum mechanical description of a molecule in an intense field is restricted to one-electron systems. Therefore, it is worthwhile to investigate complementary approaches of describing laser-molecule interactions. One such approach is based on classical

mechanics. The idea is to treat all the particles involved, not just the heavy nuclei, as classical point particles. Indeed, this type of approach was successfully introduced in atomic physics, most prominently to explain the ionization of Rydberg atoms [36,37], and was recently applied to the nonsequential double ionization of helium [38–43].

Needless to say, classical models provide a number of advantages. Foremost, the benefit is on the technical side. Since Hamilton's equations of motion are ordinary differential equations instead of partial differential equations as in the case of the time-dependent Schrödinger equation, numerical integration is straightforward. The correlated motion of a large number of particles may then be treated without approximations. Furthermore, a variety of processes such as dissociation, ionization, and electron recombination are relatively easily identified in terms of the classical trajectories of the particles involved. The probability of a specific reaction pathway may readily be obtained by counting the number of trajectories leading to a specific set of products and by comparing it with the total number of trajectories.

The problem one has to solve when constructing a classical model molecule that is self-consistent is that the initial unperturbed state of the molecule should be stable. Here self-consistent means that we want a single set of equations to describe both (i) the stationary state of the molecule before the interaction with the laser pulse and (ii) the laser-induced ionization and the subsequent motion of the electrons and protons in a laser field. An approach commonly used in cluster physics [44–46] is to include the ionization step “by hand,” by introducing an appropriate model. After an ionization event, an electron and an ion are formed from the initial neutral atom. However, in this approach the interaction between a pair of neutral atoms resulting in the formation of a bound molecule could not be described. In addition, a model molecule in which the constituent particles interact with each other only by the Coulomb interactions eventually either autodissociates, autoionizes, or collapses.

In the work on classical two- and three-electron atoms [42,43,47,48] and molecules [49], this instability is remedied by replacing the Coulomb potentials by soft-core interaction potentials, asymptotically equal to the Coulomb potentials when the distances between two particles are large enough, but finite at small distances.

^{*}Present address: Laser Technology Laboratory, RIKEN Advanced Science Institute, 2-1 Hirosawa, Wako, Saitama 351-0198, Japan; loetstedte@riken.jp

In this paper, in order to investigate the response of D_3^+ and H_3^+ to an intense, few-cycle laser pulse, we introduce a different model of a classical molecule, which is an extension of that originally presented in [50,51] and later developed and extensively applied to atomic and molecular collisions by Cohen and coworkers [52–60]. In the context of an atom-laser interaction, this type of model was adopted to investigate the double ionization of a helium atom [61,62], and the knee structure was successfully reproduced. The ionization and dissociation of H_2 and H_2^+ molecules irradiated by laser light have also been investigated by LaGattuta in Ref. [63].

The molecular ion H_3^+ (or D_3^+) is the simplest polyatomic molecule and is characterized by its triangular ground-state shape. However, laser-driven H_3^+ and D_3^+ have not been explored except the theoretical [24,29,64–67] as well as experimental [7,8] studies. On the theoretical side, the nuclear degree of freedom has not yet been accounted for, except in Refs. [24,29], where D_3^+ was irradiated with high-frequency light, and our recent work [66]. In the current study, we aim to demonstrate the capabilities of our quasiclassical model to describe laser-induced molecular dynamics and to pave the way for a future extension to larger molecules.

The paper is organized in the following way: In Sec. II, we provide a detailed definition and characterization of the model we employ for the simulation. In particular, we compare the predictions for the ground-state energy of the model H_3^+ and D_3^+ and that of quantum mechanical calculations in Sec. II B. In Sec. III, we present details of the Monte Carlo procedure used in this paper. The results of the simulations together with the discussion and explanation of the features of the angular and kinetic energy release (KER) distributions are described in Sec. IV. Section V concludes the paper.

Unless otherwise specified, we employ atomic units (a.u.) for all quantities and equations presented hereafter.

II. THEORETICAL MODEL

In our theoretical model, a momentum-dependent potential is introduced between the electron and the proton in addition to the attractive Coulomb potential. This auxiliary momentum-dependent potential is supposed to mimic the Heisenberg principle and renders the molecule stable against autoionization and dissociation. The fact that the potential depends on the momentum of the particles motivates the prefix “quasi” classical, to distinguish the model from the conventional classical systems where the potential energies depend solely on the positions of the particles. In the present investigation, there are only two electrons, and the electrons are assumed to have opposite spin for simplicity, so that spin interaction does not need to be included, but this model can be extended to many-electron problems by introducing a specific type of additional potentials to simulate the Pauli principle similar to those introduced in Refs. [51,53].

We note that similar ideas have also been employed in plasma physics [68].

A. Model potential

Before we introduce a complete Hamiltonian of the D_3^+ system, it is instructive to take a closer look at a deuterium

atom (or a hydrogen atom) in this model. The Hamiltonian reads [51]

$$H_D = \frac{1}{2}\mathbf{p}^2 + \frac{1}{2M}\mathbf{P}^2 - \frac{1}{|\mathbf{r} - \mathbf{R}|} + \frac{f(\mathbf{q}, \mathbf{s}, \xi)}{\mu(\mathbf{r} - \mathbf{R})^2}, \quad (1)$$

where M is the mass of the deuteron (or the proton), $\mu = M/(M + 1)$ is the reduced mass, and \mathbf{p} , \mathbf{r} and \mathbf{P} , \mathbf{R} are the momenta and coordinates of the electron and deuteron, respectively. For the numerical values of the deuteron and proton masses, we use $m_d = 3670.5$ and $m_p = 1836.2$. The auxiliary potential $f(\mathbf{q}, \mathbf{s}, \xi)$, a function of the relative momentum $\mathbf{q} = (\mathbf{P} - M\mathbf{p})/(M + 1)$ and the relative coordinate $\mathbf{s} = \mathbf{R} - \mathbf{r}$, is given as [51]

$$f(\mathbf{q}, \mathbf{s}, \xi) = \frac{\xi^2}{4\alpha} e^{\alpha[1 - (|\mathbf{q}|/|\mathbf{s}|)^4]}. \quad (2)$$

The meaning of $f(\mathbf{q}, \mathbf{s}, \xi)$ is the following: if the electron motion violates the constraint $|\mathbf{q}|/|\mathbf{s}| > \xi$ (the Heisenberg principle), it is repelled by the potential. The parameter α reflects the steepness of this repulsive potential. We take $\alpha = 4$ in this work, conforming with the earlier investigations [53]. For ξ , $\xi = 0.9428$ is chosen so that the minimum value of H_D equals -0.5 , the ground-state energy of a hydrogen atom.

In the same way as above, it is possible to construct both D_2^+ and D_2 molecules by introducing an auxiliary potential $f(\mathbf{q}, \mathbf{s}, \xi)$, acting between each pair of an electron and a nucleus, so that the molecules become bound and stable. However, in both cases, the equilibrium distance and the ground-state energy disagree with the quantum mechanical molecules. Cohen [53] then proposed to add certain three- and four-body potentials of the form

$$g(\mathbf{R}_1, \mathbf{R}_2, \mathbf{r}, \mathbf{P}_1, \mathbf{P}_2, \mathbf{p}) = \frac{f(\mathbf{Q}, \mathbf{S}, \chi_1)}{\nu(\mathbf{R}_1 - \mathbf{R}_2)^2}, \quad (3)$$

with $\mathbf{Q} = (\mathbf{P}_1/2 + \mathbf{P}_2/2 - 2M\mathbf{p})/(2M + 1)$, $\mathbf{S} = (\mathbf{R}_1 + \mathbf{R}_2)/2 - \mathbf{r}$, $\nu = 2M/(2M + 1)$ between two nuclei and one electron and

$$h(\mathbf{R}_1, \mathbf{R}_2, \mathbf{r}_1, \mathbf{r}_2, \mathbf{p}_1, \mathbf{p}_2) = 2 \frac{f\left(\frac{\mathbf{p}_1 - \mathbf{p}_2}{2}, \mathbf{r}_1 - \mathbf{r}_2, \chi_2\right)}{(\mathbf{R}_1 - \mathbf{R}_2)^2} \quad (4)$$

between two electrons and two nuclei. The constants $\chi_1 = 0.90$ and $\chi_2 = 1.73$ [53] are selected so that the equilibrium energies of D_2^+ and D_2 equal the quantum mechanical values. Remarkably, with this choice of potentials, the equilibrium distance is also reasonably well reproduced. The model potentials (2), (3), and (4) for D_2 and D_2^+ have been verified by Cohen [53,57–59] in the application to antiproton- H_2 and antiproton- H_2^+ collision processes.

The equilibrium nuclear configuration of D_3^+ in the electronic ground state is characterized by its geometrical structure (i.e. an equilateral triangle with internuclear distance 1.65 [69]). In the model discussed thus far, a D_3^+ (H_3^+) molecule has a ground-state energy obtained by minimizing the Hamiltonian which is 0.1 a.u. above the true value of -1.34 [69]. The corresponding equilibrium geometrical structure obtained from the model is not an equilateral triangle but an isosceles triangle. In order to further decrease the potential energy at the equilibrium nuclear configuration, a

negative five-body potential

$$w(\mathbf{R}_1, \mathbf{R}_2, \mathbf{R}_3, \mathbf{r}_1, \mathbf{r}_2, \mathbf{p}_1, \mathbf{p}_2) = -2 \frac{f\left(\frac{\mathbf{p}_1 - \mathbf{p}_2}{2}, \mathbf{r}_1 - \mathbf{r}_2, \eta\right)}{(|\mathbf{R}_1 - \mathbf{R}_2| + |\mathbf{R}_1 - \mathbf{R}_3| + |\mathbf{R}_2 - \mathbf{R}_3| + \beta)^2} \quad (5)$$

with parameters $\eta = 1.85$ and $\beta = 0.1$ is added.

After the discussion above, we are now ready to construct the complete Hamiltonian of our model D₃⁺ molecule. It reads

$$\begin{aligned} H_{D_3^+} = & \sum_{j=1}^3 \frac{\mathbf{P}_j^2}{2M} + \sum_{k=1}^2 \frac{\mathbf{p}_k^2}{2} + \frac{1}{|\mathbf{r}_1 - \mathbf{r}_2|} + \sum_{\substack{j,k=1 \\ j < k}}^3 \frac{1}{|\mathbf{R}_j - \mathbf{R}_k|} \\ & + \sum_{j=1}^3 \sum_{k=1}^2 \left[-\frac{1}{|\mathbf{R}_j - \mathbf{r}_k|} + \frac{f(\mathbf{q}_{jk}, \mathbf{s}_{jk}, \xi)}{\mu(\mathbf{R}_j - \mathbf{r}_k)^2} \right] \\ & + \sum_{\substack{j,k=1 \\ j < k}}^3 \sum_{l=1}^2 g(\mathbf{R}_j, \mathbf{R}_k, \mathbf{r}_l, \mathbf{P}_j, \mathbf{P}_k, \mathbf{p}_l) \\ & + \sum_{\substack{j,k=1 \\ j < k}}^3 h(\mathbf{R}_j, \mathbf{R}_k, \mathbf{r}_1, \mathbf{r}_2, \mathbf{p}_1, \mathbf{p}_2) \\ & + w(\mathbf{R}_1, \mathbf{R}_2, \mathbf{R}_3, \mathbf{r}_1, \mathbf{r}_2, \mathbf{p}_1, \mathbf{p}_2), \end{aligned} \quad (6)$$

where we use the notation $\mathbf{q}_{jk} = (\mathbf{P}_j - M\mathbf{p}_k)/(M+1)$ and $\mathbf{s}_{jk} = \mathbf{R}_j - \mathbf{r}_k$. There are two electrons with the coordinates $\mathbf{r}_1, \mathbf{r}_2$, and the corresponding momenta $\mathbf{p}_1, \mathbf{p}_2$, respectively, and three nuclei with the coordinates $\mathbf{R}_1, \mathbf{R}_2, \mathbf{R}_3$, and the corresponding momenta $\mathbf{P}_1, \mathbf{P}_2, \mathbf{P}_3$, respectively. Together with the specifications of the external laser field $\mathbf{E}(t)$, which we include in the dipole approximation, the Hamiltonian (6) completely determines the dynamics of the system. From a set of initial values for the momenta and the coordinates, the time evolution proceeds according to the classical equations of motion

$$\begin{aligned} \frac{d\mathbf{R}_j}{dt} &= \frac{\partial H_{D_3^+}}{\partial \mathbf{P}_j}, & \frac{d\mathbf{P}_j}{dt} &= -\frac{\partial H_{D_3^+}}{\partial \mathbf{R}_j} + \mathbf{E}(t), \\ \frac{d\mathbf{r}_k}{dt} &= \frac{\partial H_{D_3^+}}{\partial \mathbf{p}_k}, & \frac{d\mathbf{p}_k}{dt} &= -\frac{\partial H_{D_3^+}}{\partial \mathbf{r}_k} - \mathbf{E}(t), \end{aligned} \quad (7)$$

where $j = 1, 2, 3, k = 1, 2$. Note that the Hamiltonians for the hydrogen molecule and hydrogen molecular ion are expressed using Eq. (6) as $H_{D_2} = H_{D_3^+}(|\mathbf{R}_3| \rightarrow \infty, \mathbf{P}_3 = 0)$, and $H_{D_2^+} = H_{D_3^+}(|\mathbf{R}_3|, |\mathbf{r}_2| \rightarrow \infty, \mathbf{P}_3 = \mathbf{p}_2 = 0)$. A peculiarity of this model is that the momentum does not equal the mass times the velocity; that is, $d\mathbf{r}_k/dt \neq \mathbf{p}_k$ and $d\mathbf{R}_j/dt \neq \mathbf{P}_j/M$. This is because the auxiliary potentials f, g, h , and w in Eq. (6) depend on the momenta of the particles. However, at large distances \mathbf{r} , or large momenta \mathbf{p} , where the auxiliary potentials are exponentially small [$\propto \exp(-\alpha|\mathbf{r}|^4/|\mathbf{p}|^4/\xi^4)$], we recover the normal situation where the equalities $d\mathbf{r}_k/dt = \mathbf{p}_k$ and $d\mathbf{R}_j/dt = \mathbf{P}_j/M$ hold.

B. Characterization of ground state

In this section, we investigate the lowest possible total energy of the system as a function of the positions of the nuclei; that is, we investigate the potential energy surface

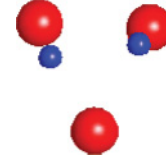


FIG. 1. (Color online) Equilibrium configuration of the model D₃⁺ molecule. Deuterons are pictured as large red spheres, and electrons as small blue spheres. If we let the origin of coordinates be located at the center of mass of the molecule, and the deuterons placed in the y - z plane, the equilibrium positions and momenta read $\mathbf{R}_1^{(eq)} = (0, 0.73, 0.45)$, $\mathbf{R}_2^{(eq)} = (0, -0.73, 0.45)$, $\mathbf{R}_3^{(eq)} = (0, 0, -0.91)$, $\mathbf{r}_1^{(eq)} = (-0.73, -0.35, 0.13)$, $\mathbf{r}_2^{(eq)} = (0.73, 0.35, 0.13)$, $\mathbf{p}_1^{(eq)} = (0.01, -1.11, -0.13)$, and $\mathbf{p}_2^{(eq)} = -\mathbf{p}_1^{(eq)}$.

(PES). To obtain the PES, we proceed exactly as in the corresponding quantum case: First, we fix the positions of the nuclei (letting $\mathbf{P}_j = 0, j = 1, 2, 3$, and $M \rightarrow \infty$). Second, we minimize the function $H_{D_3^+}$ with respect to the position and momentum vectors of the electrons, which yields the Born-Oppenheimer (BO) ground-state energy $H_{D_3^+}^{\min} = \epsilon$. In the equilibrium configuration, the electrons have both fixed positions and fixed momenta, $d\mathbf{r}_k/dt = \mathbf{0}, k = 1, 2$. Repeating the above procedure for different nuclear positions, we obtain the PES of the molecule. Note that the Hamiltonian (6) is invariant with respect to an overall rotation of all momentum vectors. The equilibrium configuration with the minimum BO energy in our model, shown schematically in Fig. 1, is an isosceles triangle with side lengths 1.46 and 1.55 and energy $\epsilon_0 = -1.342$. This is to be compared with the exact, quantum mechanical equilibrium ground state BO energy $\epsilon_0^{\text{quant}} = -1.344$ [69], which is obtained at the equilibrium geometrical structure of an equilateral triangle with nuclear separation 1.65.

In Fig. 2 we show the comparison between the quantum mechanical PES and that obtained by the current model (6). For the numerical minimization of the Hamiltonian (6), we use the downhill simplex method described in Ref. [70]. In order to confirm that the real, global energy minimum was found, trials of the search are repeated several times with different initial guesses of the coordinates and momenta of the particles. The

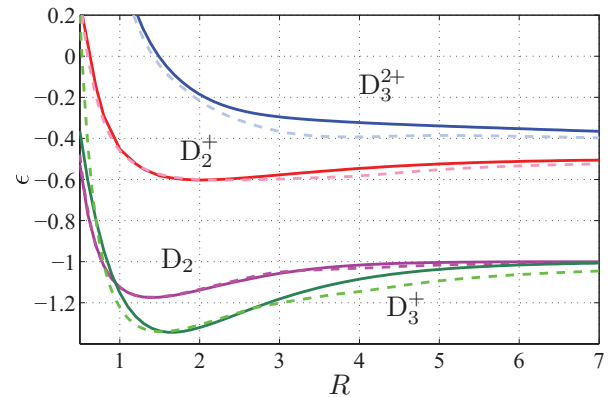


FIG. 2. (Color online) Quantum mechanical ground-state energy in a.u. (drawn with solid lines) and the PES in a.u. obtained from minimization of the Hamiltonian (6) (drawn with dashed lines). R denotes the distance in a.u. between the nuclei. For D₃²⁺ and D₃⁺ the equilateral triangle configurations are assumed.

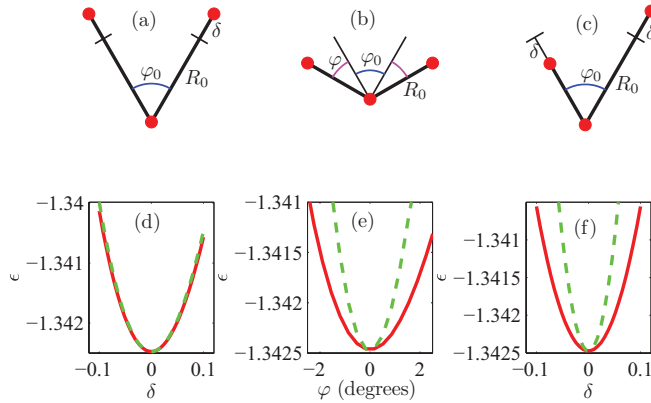


FIG. 3. (Color online) Comparison between three different cuts in the PES (in a.u.) of the D_3^+ molecule, calculated with GAMESS (HF, 6-311G basis set: solid lines), and with the model Hamiltonian (6) (dashed lines). Panels (a), (b), and (c) define the positions of the nuclei with respect to the equilibrium configuration of the respective model, with δ and R_0 measured in a.u., and φ and φ_0 in degrees. Since the HF approximation used for the quantum calculation yields a minimum energy slightly higher (0.07) than the exact ground-state energy from Ref. [69], the solid curves in panels (d), (e), and (f) are shifted vertically so that the curves agree at the minimum energy.

quantum mechanical values for D_2 were taken from Ref. [71], and those for D_2^+ from Ref. [72]. The potential energy curve for D_3^+ was obtained by fitting the data taken from Ref. [69] to a Morse-type potential. GAMESS [73] (6-311G basis set) was used to obtain the potential energy curve for D_3^{2+} .

It can be seen in Fig. 2 that all the model curves are in close agreement with the quantum ones. Indeed, for all the curves in Fig. 2, the difference $|\epsilon^{\text{model}}(R) - \epsilon^{\text{qm}}(R)|$ between the model curve and the quantum mechanical curve is smaller than 0.1 when $R > 1$. For D_2 , the equilibrium internuclear distance obtained by the model Hamiltonian (6) is $R_{\text{eq}}^{\text{model}}(D_2) = 1.39$, which is in good agreement with the quantum mechanical value $R_{\text{eq}}^{\text{qm}}(D_2) = 1.4$ [71]. For D_2^+ , we have $R_{\text{eq}}^{\text{model}}(D_2^+) = 2.3$, compared to $R_{\text{eq}}^{\text{qm}}(D_2^+) = 2.0$ [72]. Of course, perfect agreement could not be expected, but considering that the KER spectra were qualitatively reproduced (see Sec. IV C), the present model should be sufficiently good for achieving qualitative agreement with experimental data.

The comparison between the ground state obtained by the quantum chemical calculation and that obtained by the present model around the equilibrium nuclear configuration is shown in Fig. 3. In this figure, we show one-dimensional cuts of the PES of D_3^+ , slightly displaced from the minimum-energy configuration along the directions defined in Figs. 3(a), 3(b), and 3(c). For the symmetric stretching mode [panels (a) and (d) in Fig. 3], the model and quantum calculation are in almost perfect agreement. Fitting of the potential energy to an expression

$$\epsilon = \epsilon_0 + \frac{1}{2}F\delta^2, \quad (8)$$

with the frequency parameter F gives $F^{\text{model}} = 0.45$ for the model, and $F^{\text{HF}} = 0.43$ for the quantum Hartree-Fock (HF) calculation. Fitting the curve of the asymmetric stretching mode shown in Figs. 3(c) and 3(f) results in $F^{\text{model}} = 1.2$ and $F^{\text{HF}} = 0.38$. For the bending mode in Figs. 3(b) and 3(e),

we employ the fitting expression

$$\epsilon = \epsilon_0 + \frac{1}{2}R_0^2F_\varphi(\varphi - \varphi_0)^2, \quad (9)$$

with φ and φ_0 expressed in radians, and obtain $F_\varphi^{\text{model}} = 1.56$ and $F_\varphi^{\text{HF}} = 0.49$. In both Eqs. (8) and (9), $\epsilon_0 = -1.342$ for the model and $\epsilon_0 = -1.28$ for the HF calculations. It thus seems that the model ground state is more stiff both along the asymmetric stretching coordinate and along the bending coordinate; that is, the model molecule is more difficult to be bent and stretched asymmetrically than the corresponding quantum ground state. As we will see in Sec. IV C, this is probably the reason for the disagreement between the calculated kinetic energy release distributions and the experimentally measured ones. For a given vibrational energy, the average internuclear distance of the model is estimated to be only $2/3$ of the corresponding quantum system, which results in overestimation of the kinetic energy release after the Coulomb explosion by a factor of 1.5.

III. SIMULATION

In this section we present some details of the simulation of a D_3^+ molecule and a H_3^+ molecule submitted to an intense short laser pulse. The simulation procedure consists of three steps: sampling of initial values, numerical integration of the particle trajectories, and identification of the final state. First, initial values for the momenta and positions at $t = 0$ are given by a sampling algorithm described in more detail in Appendix A. Then, in order to derive the temporal evolution of the momenta and positions of the particles, the equations of motion (7) are solved numerically using an adaptive fifth-order Runge-Kutta solver. The numerical errors in the solutions of the equations of motion are further discussed in Appendix B.

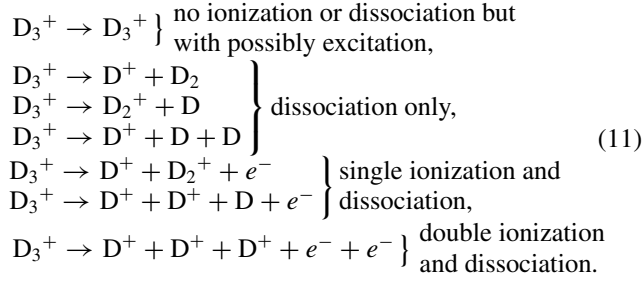
We employ a standard sine-square pulse for the laser field $\mathbf{E}(t) = \hat{\mathbf{E}}E(t) = (0, 0, E(t))$, with the polarization vector $\hat{\mathbf{E}}$ pointing in the z direction, and

$$E(t) = \begin{cases} E_0 \sin^2\left(\frac{\pi}{T}t\right) \sin \omega_0 t & \text{if } 0 \leq t \leq T \\ 0 & \text{if } t < 0 \text{ or } t > T, \end{cases} \quad (10)$$

where $T = 2\pi N/\omega_0$ is the total duration, N is the number of cycles, and ω_0 is the laser frequency. Throughout the paper we let $\omega_0 = 5.8 \times 10^{-2}$, corresponding to the wavelength of 790 nm, and $N = 3$, corresponding to the pulse duration $T = 7.8$ fs, which implies a 3.9 fs full width at half maximum (FWHM) of the electric field envelope. For a laser pulse with a sine-square envelope, the FWHM of the electric field is related to the pulse duration as $\text{FWHM} = T/2$, while for the intensity envelope we have instead $\text{FWHM} \approx T/2.75$. For the conversion to the laser field intensities we use the formula $I [\text{W}/\text{cm}^2] = 3.51 \times 10^{16} E_0^2 [\text{a.u.}]$. The laser parameters are taken to be similar to those in Ref. [7], where a 7 fs (intensity envelope FWHM), 790 nm pulse with laser field intensities in the range $10^{14} \sim 10^{16} \text{ W}/\text{cm}^2$ was employed.

The simulation is run until the final state of the system can be identified. The propagation time required was found to be at least $T + 10^3$ a.u. and was in most cases much longer. From the initial D_3^+ molecule, the following seven kinds of decomposition pathways are identified after the interaction

with the light pulse.



There may also exist the dissociation pathway $\text{D}_3^+ \rightarrow \text{D}^- + \text{D}^+ + \text{D}^+$ because the present model gives a positive electron affinity $\epsilon_a(\text{D}) = \epsilon_0(\text{D}) - \epsilon_0(\text{D}^-)$ for a deuterium atom as $\epsilon_a(\text{D}) = 1/[16\xi^2(1 + 1/2\alpha)] \approx 0.063$ [51], which is comparable with, but higher than the accurate theoretical quantum mechanical value of $\epsilon_a(\text{D}) = 0.028$ [74]. However, the yield of this pathway should be very small, because $\epsilon_a(\text{D})$ is sufficiently small so that any perturbation induced by either the laser field or nearby particles will easily ionize D^- into $\text{D} + e^-$. In the simulations, evidence for the pathway $\text{D}_3^+ \rightarrow \text{D}^- + \text{D}^+ + \text{D}^+$ was found for only one trajectory out of 4×10^4 for the simulations performed at the light field intensity 4×10^{15} W/cm². Therefore, this pathway whose relative yield is estimated to be less than 10^{-4} will not be considered in the present investigation.

The assignment of the final products at the end of the run is made automatically based on the distance between the fragments and the total energy of the electrons. Two fragments are considered to be dissociated if the distance between them exceeds 10 and does not become smaller than 10 again. Even when the distance becomes larger than 10, it could become smaller again if the final fragments are in a vibrationally highly excited state. Therefore, we run the simulation for sufficiently long time so that the final pathway can be securely identified. An electron k is considered to be completely separated from nuclei (i.e., ionization is considered to occur) if the single-particle energy $\epsilon_k^{(e)}$ of the electron is positive, where $\epsilon_k^{(e)}$ is defined as

$$\begin{aligned}
 \epsilon_k^{(e)} = & \frac{\mathbf{p}_k^2}{2} + \sum_{j=1}^3 \left[\frac{-1}{|\mathbf{R}_j - \mathbf{r}_k|} + \frac{f(\mathbf{q}_{jk}, \mathbf{s}_{jk}, \xi)}{\mu(\mathbf{R}_j - \mathbf{r}_k)^2} \right. \\
 & \left. + \sum_{\substack{j,l=1 \\ j < l}} g(\mathbf{R}_j, \mathbf{R}_l, \mathbf{r}_k, \mathbf{p}_j, \mathbf{p}_l, \mathbf{p}_k) \right] \\
 & + \frac{1}{2} \left[\frac{1}{|\mathbf{r}_1 - \mathbf{r}_2|} + \sum_{j < l} h(\mathbf{R}_j, \mathbf{R}_l, \mathbf{r}_1, \mathbf{r}_2, \mathbf{p}_1, \mathbf{p}_2) \right. \\
 & \left. + w(\mathbf{R}_1, \mathbf{R}_2, \mathbf{R}_3, \mathbf{r}_1, \mathbf{r}_2, \mathbf{p}_1, \mathbf{p}_2) \right]. \quad (12)
 \end{aligned}$$

In the above definition (12), we adopt the convention that the electron-electron repulsion energy as well as the quasiclassical potential energies h and w that depend on the coordinates and momenta of both electrons are split equally into the two electrons. The contribution from the auxiliary potentials f , g , h , and w to the electron energy $\epsilon_k^{(e)}$ are negligible once an electron is ejected.

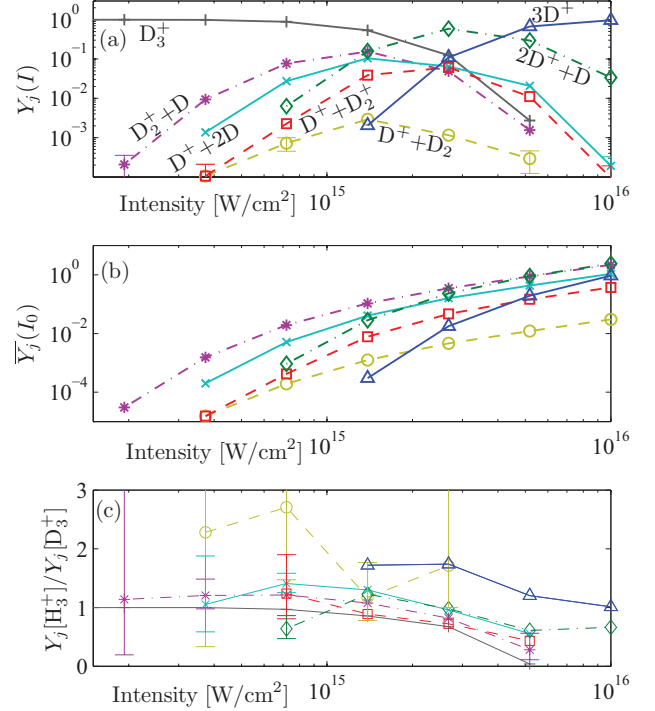


FIG. 4. (Color online) (a) Relative yields for the seven possible pathways, for the D_3^+ molecule: D_3^+ (+), $\text{D}_2^+ + \text{D}$ (*), $\text{D}^+ + 2\text{D}$ (×), $\text{D}^+ + \text{D}_2$ (○), $\text{D}^+ + \text{D}_2^+$ (□), $2\text{D}^+ + \text{D}$ (◇), and 3D^+ (△). (b) Yields from (a) integrated over a three-dimensional Gaussian beam [see Eq. (15)]. (c) The ratio between the H_3^+ and D_3^+ yields. The error bars in (a) and (c) are statistical, and are shown when they exceed the size of the curve symbol.

In the way described above, many trajectories with slightly different initial conditions were run, and the final states were assigned for the respective runs. The total yields of the respective decomposition pathways are then obtained by dividing the number of trajectories that ended up in the respective final state by the total number of the trajectories calculated.

IV. RESULTS

A. Total probabilities

According to the procedure described in Sec. III, simulations were carried out at eight different laser intensities ranging from 10^{14} to 10^{16} W/cm² for both D_3^+ and H_3^+ . Experimentally, D_3^+ is preferred, since the HD^+ contamination can be avoided in the ion beam [7,8]. We therefore concentrate on D_3^+ and show the results for D_3^+ in more detail, although the results for H_3^+ are also shown if necessary for comparison.

The relative yields of the respective dissociation pathways thus obtained are shown in Fig. 4. Approximately a total of 10^4 trajectories were run for each intensity. The relative yield Y_j for the reaction pathway j is given by

$$Y_j = \frac{n_j}{n_{\text{tot}}}, \quad (13)$$

where n_j denotes the number of trajectories that ended up in the final pathway j , and n_{tot} is the total number of the

trajectories and is defined as $n_{\text{tot}} = \sum_j n_j$. The ranges of the statistical errors $-\sigma_j \sim +\sigma_j$ shown in Fig. 4(a) are calculated by the formula

$$\sigma_j = \sqrt{\frac{n_j(n_{\text{tot}} - n_j)}{n_{\text{tot}}^3}}, \quad (14)$$

obtained from the standard deviation of the binomial distribution divided by n_{tot} . In the limit $n_j \ll n_{\text{tot}}$, we have $\sigma_j = \sqrt{n_j}/n_{\text{tot}}$. In Fig. 4, we see that all the seven kinds of final states are produced in the simulation, indicating that the model successfully describes both ionization and dissociation. The yields of the three pathways in which only dissociation proceeds without ionization, $\text{D}^+ + \text{D}_2$, $\text{D}^+ + 2\text{D}$, and $\text{D}_2^+ + \text{D}$, take a maximum at a certain intensity around 10^{15} W/cm² and decrease at the higher laser field intensities associated with the increase in the yields of the ionization. At the highest laser field intensity of 10^{16} W/cm², double ionization followed by the three-body Coulomb explosion ($\text{D}^+ + \text{D}^+ + \text{D}^+ + e^- + e^-$) has the largest yield of $Y_j = 0.97$, compared to $Y_j = 0.03$ for the $2\text{D}^+ + \text{D}$ pathway. Evidently, at the very large intensity, the yield of this double ionization pathway should become unity. We note that quantitative comparison with experimental results [7] of this kind of yield-vs-intensity measurement is difficult since the experimental results carry the light focal volume effect [75]. In order to compare our theoretical results with experimental data, we integrate the intensity-dependent yields $Y_j(I)$ over a three-dimensional (3D) Gaussian beam profile to obtain $\bar{Y}_j(I_0)$,

$$\bar{Y}_j(I_0) = -\frac{1}{V_f} \int_0^{I_0} Y_j(I) \frac{dV(I)}{dI} dI, \quad (15)$$

normalized by the focal volume V_f . In Eq. (15), I_0 is the peak intensity of the light field and $V(I)$ is the volume where the intensity is larger than I [75]. For the intensity distribution, we have used the standard expression [75] $I(r, z) = I_0(1 + z^2/z_R^2)^{-1} \exp[-2r^2w_0^{-2}(1 + z^2/z_R^2)^{-1}]$, where w_0 is the beam waist and z_R is the Rayleigh length. This results in the expression $V(I) = V_f[(4/3)\beta + (2/9)\beta^3 - (4/3)\arctan \beta]$, with $V_f = \pi w_0^2 z_R$ and $\beta = (I_0/I - 1)^{1/2}$ [76]. In this averaging procedure, it is assumed that the size of the ion beam is much larger than the laser focal volume. The quantity $\bar{Y}_j(I_0)$ is shown in Fig. 4(b), in which the volume-averaged yields for all the pathways exhibit a monotonic increase as the laser field intensity increases. At peak intensity $I_0 = 10^{16}$ W/cm², the $2\text{D}^+ + \text{D}$ pathway has the largest value of $\bar{Y}_j(I_0)$, which is in agreement with experiment [7]. However, the calculated relative yields of the $\text{D}^+ + \text{D}_2^+$ and $\text{D}^+ + \text{D}_2$ pathways are one order of magnitude smaller than the experimentally measured yields, while the calculated relative yield of the $\text{D}^+ + 2\text{D}$ pathway is too large by roughly one order of magnitude. We conclude that, to quantitatively reproduce experimentally measured total yields, it is necessary to improve the model Hamiltonian (6). Besides the light focal volume effect and limitations of the model Hamiltonian (6), the different pulse durations used in the simulation (3 fs intensity FWHM) and the experiment (7 fs intensity FWHM) also contribute to the discrepancies of the intensity-averaged relative yields $\bar{Y}_j(I_0)$ with the experimental data in [7].

The results of the simulation for H_3^+ were found to be very similar to those of D_3^+ . For the comparison, the ratio of the yields; that is, the yield of Y_j for H_3^+ with respect to Y_j for D_3^+ , is plotted for each pathway in Fig. 4(c). For the ratio of the yields, the range of the error $-\sigma_j^- \sim +\sigma_j^+$ was estimated as

$$\sigma_j^\mp = \mp \frac{Y_j[\text{H}_3^+] \mp \sigma_j[\text{H}_3^+]}{Y_j[\text{D}_3^+] \pm \sigma_j[\text{D}_3^+]} \pm \frac{Y_j[\text{H}_3^+]}{Y_j[\text{D}_3^+]}, \quad (16)$$

where σ_j is evaluated by Eq. (14). The general trend is that the ratio $Y_j[\text{H}_3^+]/Y_j[\text{D}_3^+]$ decreases for all pathways as the laser intensity increases. For the double-ionization pathway the ratio decreases from $Y_j[\text{H}_3^+]/Y_j[\text{D}_3^+] = 1.7$ at $I = 1.4 \times 10^{15}$ W/cm² to $Y_j[\text{H}_3^+]/Y_j[\text{D}_3^+] = 1.0$ at $I = 10^{16}$ W/cm². This decrease in the ratio $Y_j[\text{H}_3^+]/Y_j[\text{D}_3^+]$ can be ascribed to the lighter mass of H, leading to the larger values of the average internuclear distance of the intermediate H_3^{2+} molecular ion compared to D_3^{2+} as will be discussed in detail in Sec. IV C1. The results in Fig. 4(c) show that H_3^+ is easier to be doubly ionized than D_3^+ at the laser field intensities of around 10^{15} W/cm². This implies that the ionization probability is enhanced for the larger internuclear distances. The enhancement of the ionization at the large internuclear distance of classical molecular systems has also been reported previously [49,77]. For the larger intensities, the enhanced ionization is less pronounced, as seen in Fig. 4(c). This is because the molecule is easily ionized regardless of the internuclear distance, and the ratio $Y_j[\text{H}_3^+]/Y_j[\text{D}_3^+]$ tends to become unity.

B. Angular distributions

1. Distributions in θ and χ

We now turn to investigate the dependence of the yields of the decomposition pathways on the directions of the final momenta of the fragments. We first define the two angles θ and χ , which are relevant for the three-body-breakup pathways 3D^+ , $2\text{D}^+ + \text{D}$, and $\text{D}^+ + 2\text{D}$ [7]. The angle θ is defined as the angle between the laser field polarization vector and the normal vector of the plane spanned by the final momentum vectors of the protons,

$$\cos \theta = \hat{\mathbf{z}} \cdot \hat{\mathbf{n}}, \quad \hat{\mathbf{n}} = \frac{\mathbf{P}_1^{\text{fin}} \times \mathbf{P}_2^{\text{fin}}}{|\mathbf{P}_1^{\text{fin}} \times \mathbf{P}_2^{\text{fin}}|}, \quad (17)$$

as seen in the graphical explanation of Fig. 5(e). Because \mathbf{n} can equivalently be defined as the vectorial product of “ $\mathbf{P}_1^{\text{fin}}$ and $\mathbf{P}_3^{\text{fin}}$ ” or “ $\mathbf{P}_2^{\text{fin}}$ and $\mathbf{P}_3^{\text{fin}}$,” we employ an average $\hat{\mathbf{n}} = \hat{\mathbf{n}}_{\text{av}} \equiv \frac{1}{3} \sum_{j < k} \mathbf{P}_j^{\text{fin}} \times \mathbf{P}_k^{\text{fin}} / |\mathbf{P}_j^{\text{fin}} \times \mathbf{P}_k^{\text{fin}}|$ in the simulation. As an alternative to using the momenta \mathbf{P}_j , we may define $\hat{\mathbf{n}}$ in terms of the velocities $d\mathbf{R}_j/dt = \dot{\mathbf{R}}_j$ as $\hat{\mathbf{n}} = (\dot{\mathbf{R}}_1^{\text{fin}} \times \dot{\mathbf{R}}_2^{\text{fin}}) / |\dot{\mathbf{R}}_1^{\text{fin}} \times \dot{\mathbf{R}}_2^{\text{fin}}|$. We have checked that this alternative definition does not change the curves shown in Figs. 5 and 6. A similar remark holds for the angle χ , defined in Eq. (18), the angle ϕ , defined in Eq. (19), and the kinetic energy release, defined in Eq. (20). The angle χ denotes the angle between the projection $\hat{\mathbf{E}}_{\text{proj}}$ of the laser polarization vector on the plane perpendicular to $\hat{\mathbf{n}}$ and the momentum of one of the outgoing deuterons or deuterium atoms,

$$\cos \chi = \hat{\mathbf{E}}_{\text{proj}} \cdot \frac{\mathbf{P}_j^{\text{fin}}}{|\mathbf{P}_j^{\text{fin}}|}, \quad \hat{\mathbf{E}}_{\text{proj}} = \frac{\hat{\mathbf{E}} - (\hat{\mathbf{E}} \cdot \hat{\mathbf{n}})\hat{\mathbf{n}}}{|\hat{\mathbf{E}} - (\hat{\mathbf{E}} \cdot \hat{\mathbf{n}})\hat{\mathbf{n}}|}. \quad (18)$$

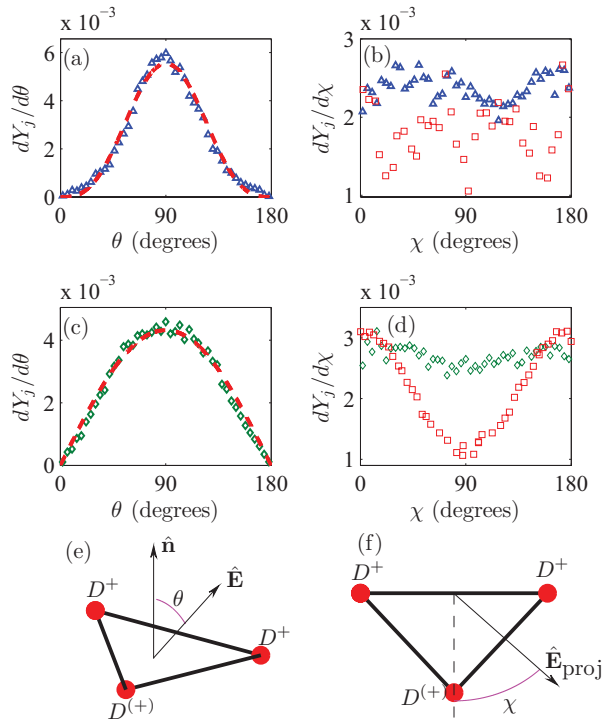


FIG. 5. (Color online) Final angular distributions for pathways $3D^+$ [Δ , panels (a) and (b)], and $2D^+ + D$ [\diamond , panels (c) and (d)], at intensity $4 \times 10^{15} \text{ W/cm}^2$. The angles θ and χ are defined in Eqs. (17) and (18), respectively. For a particular pathway j , the differential yield in bin k is defined as $dY_j/d\theta = n_k^j/(n_{\text{tot}}\Delta)$, where n_k^j is the number of trajectories in bin k , and Δ is the bin size. The statistical error bars are everywhere smaller than the symbol size. The red dashed line in panel (a) is a $\sin^3 \theta$ fit, and the red dashed line in panel (b) is a $\sin \theta$ fit to the numerically obtained data. In panels (b) and (d), experimental data (\square) from Ref. [7] for 7 fs, 10^{16} W/cm^2 laser pulses are shown. The experimental curves were normalized to the theoretical curves at the maximal value of the theoretical curve.

In the case of the $2D^+ + D$ pathway, \mathbf{P}^{fin} is the final momentum vector of the D atom, while in the case of the $D^+ + 2D$ pathway, \mathbf{P}^{fin} is the final momentum vector of the D^+ ion. The definition of χ is shown pictorially in Fig. 5(f).

In Fig. 5, we show the distributions of the angles θ and χ for the pathways $2D^+ + D$ and $D^+ + D^+ + D^+$ at the peak laser field intensity of $4 \times 10^{15} \text{ W/cm}^2$ (corresponding to the peak electric field of $E_0 = 0.34$). In order to improve statistics, $n_{\text{tot}} = 4 \times 10^4$ runs were performed at this particular intensity, to be compared with $n_{\text{tot}} = 10^4$ used for the total yields presented in Fig. 4. In Fig. 6, we display the corresponding quantities for the lower intensity $1.4 \times 10^{15} \text{ W/cm}^2$ (corresponding to $E_0 = 0.2$), where $n_{\text{tot}} = 6 \times 10^4$ runs were simulated.

Experimental data of the θ and χ distributions for the $3D^+$ and $2D^+ + D$ pathways, corresponding to Figs. 5 and 6(a)–6(d), were reported in Ref. [7]. In Ref. [7], a $\sin^3 \theta$ dependence for the θ distribution was found for both $3D^+$ and $2D^+ + D$, which is in good agreement with Fig. 5(a), and Figs. 6(a) and 6(c) in the present study. Concerning the θ distributions, we note that an ensemble of molecules whose spatial orientations are randomly distributed would give

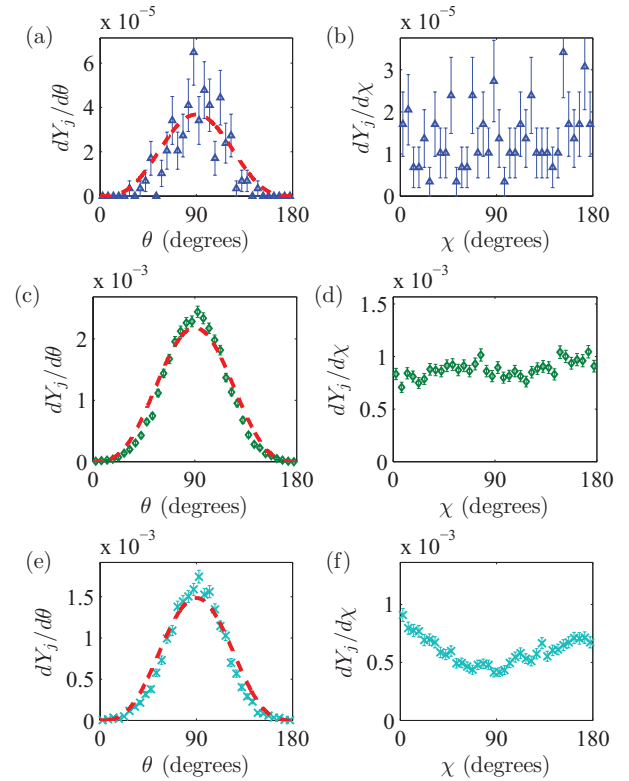


FIG. 6. (Color online) Final angular distributions for pathways $3D^+$ [panels (a) and (b)], $2D^+ + D$ [panels (c) and (d)], and $D^+ + 2D$ [panels (e) and (f)], at lower intensity $1.4 \times 10^{15} \text{ W/cm}^2$. The angles θ and χ are defined in Eqs. (17) and (18), respectively. The error bars represent statistical uncertainties. The red dashed lines in panels (a), (c), and (e) are $\sin^3 \theta$ fits to the numerically obtained data.

rise to a $\sin \theta$ distribution, if all directions of the molecular plane relative to the laser field vector have equal ionization probability. This is simply because, when the polarization direction of the laser field is fixed in space to the polar axis, the probability of finding a vector with the polar angle $\theta \pm d\theta$ and the azimuth angle $\varphi \pm d\varphi$ is proportional to the surface element of the sphere, $\sin \theta d\theta d\varphi$. Therefore, in the limit of laser intensity $I \rightarrow \infty$, where the molecular structure becomes unimportant and ionization is equally probable in all directions, the distribution necessarily approaches a $\sin \theta$ shape. This is what we find for the $2D^+ + D$ pathway as shown in Fig. 5(c), for the higher intensity $4 \times 10^{15} \text{ W/cm}^2$. We have also shown that the θ distribution for the double ionization pathway $3D^+$ becomes a $\sin \theta$ -type distribution at the highest intensity of 10^{16} W/cm^2 .

It should be noted that interesting patterns were found in the χ distributions in experiment, such as a star-like χ distribution for the $3D^+$ pathway. For reference, the experimental χ distributions from Ref. [7] for the $3D^+$ and $2D^+ + D$ pathways are shown in Figs. 5(b) and 5(d), respectively. In our simulation, we were not able to find such χ distributions. As seen in Figs. 5(b) and 5(d) and in Figs. 6(b), 6(d), and 6(f), the simulated results exhibit rather flat distributions in χ . It is therefore possible that the star-like patterns found in Ref. [7] in the χ distribution originate from quantum interference,

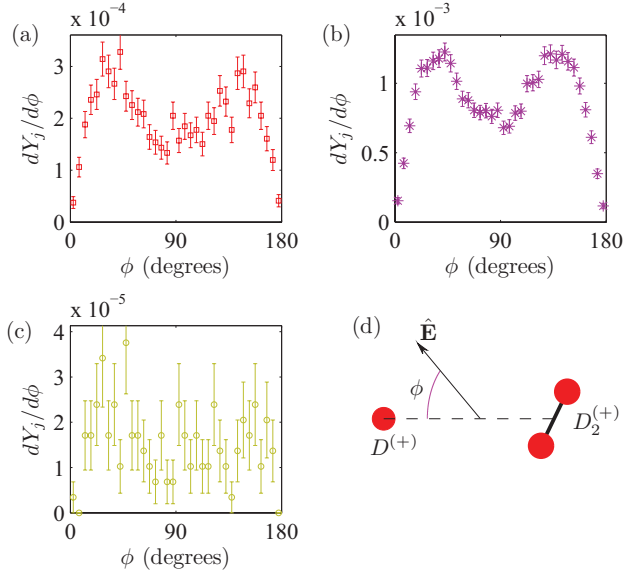


FIG. 7. (Color online) Final distributions in the angle ϕ for pathways $D^+ + D_2^+$ (a), $D_2^+ + D$ (b), and $D^+ + D_2$ (c), at intensity 1.4×10^{15} W/cm². The angle ϕ is explained in panel (d). The error bars represent statistical uncertainties.

which could not be described by the present quasiclassical model.

2. Distributions in ϕ

In the pathways where a D_2 molecule or a D_2^+ molecular ion is produced, there is only one relevant angle, ϕ . We take this angle to be the angle between the laser polarization vector and the final momentum vector of the deuteron (or the deuterium atom),

$$\cos \phi = \hat{\mathbf{E}} \cdot \frac{\mathbf{P}^{\text{fin}}}{|\mathbf{P}^{\text{fin}}|}, \quad (19)$$

where \mathbf{P}^{fin} is the final momentum vector of D for the $D_2^+ + D$ pathway or that of D^+ for the $D^+ + D_2^+$ and $D^+ + D_2$ pathways. The angular distributions for the $D^+ + D_2^+$, $D_2^+ + D$, and $D^+ + D_2$ pathways at the intensity of 1.4×10^{15} W/cm² are shown in Fig. 7. For the $D^+ + D_2^+$ and $D_2^+ + D$ pathways [Figs. 7(a) and 7(b)], a double-hump structure with peaks at $\phi = 40^\circ$ and 140° is seen. Even though the statistics are not good for the $D^+ + D_2$ pathway [Fig. 7(c)], a double-peak structure in the ϕ distribution can vaguely be seen. It can be said that this double-peak structure is a characteristic feature commonly seen in the pathways through which a D_2 or D_2^+ molecule is produced in the final state. Because the angular distributions for the H_3^+ simulations were found to be very similar to those of D_3^+ , we only showed here the distributions calculated for D_3^+ .

C. Kinetic energy release distributions

1. KER spectra at high field intensity

The distributions of the KER for the three ionization pathways ($D^+ + D_2^+ + e^-$, $2D^+ + D + e^-$, and $3D^+ + 2e^-$) are plotted in Fig. 8. The KER is defined as the sum of the

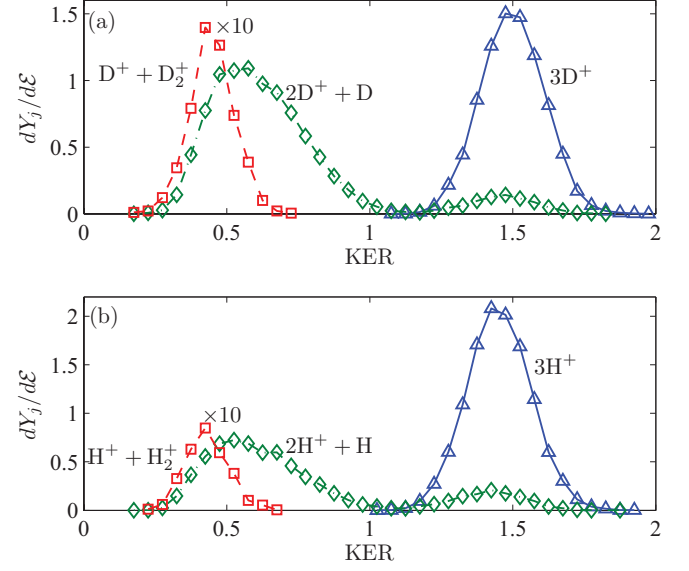


FIG. 8. (Color online) Kinetic energy release (in a.u.) for the three ionization pathways, for (a) D_3^+ and (b) H_3^+ , at intensity 4×10^{15} W/cm². Each point corresponds to an energy bin. The statistical error bars are of the same size or smaller than the curve symbols. Note that the curve for the $D^+ + D_2^+$ pathway has been multiplied by a factor of 10 for visualization purposes.

kinetic energy of the deuterons at the end of the trajectory,

$$\text{KER} = \sum_{i=1}^3 \frac{(\mathbf{P}_i^{\text{fin}})^2}{2M}. \quad (20)$$

The kinetic energies of the bound electrons are negligibly small compared to the total kinetic energy and, therefore, they are not included in the definition (20). The kinetic energy of the ejected electrons is not included in the definition (20) either, but can of course be considered separately. Since the electron spectra were not measured in Ref. [7], we concentrate on the KER distributions of a deuteron in the present paper. We note that, even though the curves shown in Fig. 8 are calculated at a particular laser field intensity, we showed in our previous investigation [66] that the KER distributions do not change significantly after intensity volume averaging. For the D_3^+ data shown in Fig. 8(b), after intensity averaging the peak positions of the $D^+ + D_2^+$ and $2D^+ + D$ curves were shifted with approximately 0.1 a.u. toward lower energy, while the widths were unchanged. For the $3D^+$ curve, the peak position was unchanged, and the FWHM was broadened by approximately 0.1 a.u.

As compared in Fig. 8, the results for D_3^+ and H_3^+ are found to be very similar. The only difference is that the sum of the relative yields of the double ionization pathway for H_3^+ is about twice as large as the single-ionization pathway $2H^+ + H$, while they are comparable for D_3^+ . It can also be seen that the peak energy for the $3H^+$ pathway is slightly lower in energy than that for $3D^+$. This reflects the fact that the protons having the lighter mass are more spread than the deuterons. Indeed, for the $3D^+$ pathway, the distribution of the average internuclear distance $R_{\text{av}} = \sum_{j < k} |\mathbf{R}_j - \mathbf{R}_k|/3$ at the moment of the ejection of the second electron is peaked at $R_{\text{av}} = 2.2$ with a FWHM of 0.4, while for the $3H^+$ pathway,

the ejection of the second electron occurs at $R_{av} = 2.4$ with a FWHM of 0.6.

As has already been discussed in our previous paper [66], it is found for the three ionization pathways that the KER distributions obtained by the present simulation are higher than the corresponding experimental distributions [7] by about 50%, while the shapes of the distribution curves were well reproduced by the simulation. For the three ionization pathways both the relative energies of the KER peaks and the relative widths of the peaks are well reproduced by the simulation. For example, the peak energy of the KER distribution of the 3D⁺ pathway was observed at about 1 at the peak laser field intensity 10^{16} W/cm², while the peak position in our simulation is at 1.5 as shown in Fig. 8. This overestimation of the KER may be ascribed to the model potentials in Eq. (6). As seen in Fig. 3, the ground state PES for D₃⁺ adopted in the simulation is too steep. Indeed, the force constants of the two vibrational modes out of the three are three times as large as the theoretical ones calculated by quantum chemical methods. Because of the steep potential, the internuclear distances could not become sufficiently large, resulting in the overestimation of the KER. Therefore, in order to reproduce the experimental KER distributions more quantitatively, it is at least necessary to adjust more the ground state PES.

2. High-energy KER peak in the 2D⁺ + D pathway

In both Figs. 8(a) and 8(b), the single ionization pathway 2D⁺ + D exhibits a small peak at KER ~ 1.5 . This kind of high KER for the decomposition pathway accompanying neutral fragments has been observed previously for laser-induced dissociation of H₂ [78–80], where the mechanism was called “frustrated tunneling ionization,” in which one electron escapes first from the Coulomb attractive potential through tunneling, and then recombines with the proton to form a highly excited H atom in a Rydberg state. The peak at KER ~ 1.5 in Fig. 8 can also be explained in a similar manner, but the first tunneling step needs to be replaced by the over-the-barrier escape because our model based on classical mechanics does not describe tunneling. Our simulation thus suggests that this type of Rydberg state formation exists also in the decomposition of polyatomic molecules in the over-the-barrier regime.

In order to support the intuitive explanation above, an example of a trajectory leading to a high KER (KER = 1.4), with a bound electron in the final state is shown in Fig. 9. This trajectory reveals that the eventually bound electron first escapes from the atomic or molecular zone and travels very far, over 100 a.u., before recombining into the bound state just before the end of the pulse.

By collecting all the trajectories of this kind, we find that the energy distribution of the loosely bound electron in the final state forms a broad peak centered at $\varepsilon^{(e)} = -0.02$ with a peak width of $\Delta\varepsilon^{(e)} = 0.02$ (FWHM). In terms of the principal quantum number $n = \sqrt{-1/(2\varepsilon^{(e)})}$, this corresponds to $4 \leq n \leq 7$.

We note that excited D (or H) atoms can be directly detected experimentally as shown in Ref. [78]. In particular, both over-the-barrier and tunneling ionization [81] of the excited atoms by a guiding electric field (of order ≈ 200 V/cm) often used in experiments are negligible.

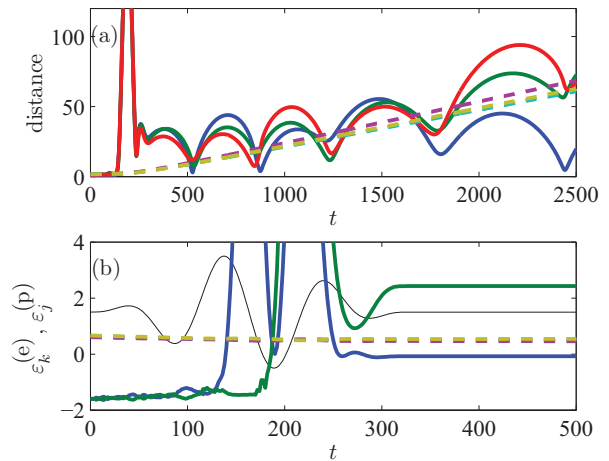


FIG. 9. (Color online) (a): The solid lines show the time evolution (with t measured in a.u.) of the distances $|\mathbf{R}_1 - \mathbf{r}_{\text{bound}}|$, $|\mathbf{R}_2 - \mathbf{r}_{\text{bound}}|$, and $|\mathbf{R}_3 - \mathbf{r}_{\text{bound}}|$ (in a.u.) of the eventually bound electron from the three deuterons, while the dashed lines show the three internuclear distances $|\mathbf{R}_1 - \mathbf{R}_2|$, $|\mathbf{R}_1 - \mathbf{R}_3|$, and $|\mathbf{R}_2 - \mathbf{R}_3|$ (in a.u.). (b): Solid lines depict the single particle electron energies $\varepsilon_k^{(e)}$, $k = 1, 2$ (in a.u.), defined in Eq. (12). Dashed lines show the single particle energies $\varepsilon_j^{(p)}$, $j = 1, 2, 3$ (in a.u.), of the protons, defined as $\varepsilon_j^{(p)} = \mathbf{P}_j^2/2M + (1/2)\sum_{j \neq k} 1/|\mathbf{R}_j - \mathbf{R}_k|$. The electric field of the laser (not to scale, and shifted) is shown with a thin line for reference. The laser parameters are the same as in Fig. 8.

The existence of this type of high-energy peak for the 2D⁺ + D pathway was not identified in the experimentally observed KER spectrum when the laser pulse width was 7 fs [7], but was identified later when the laser pulse width was 40 fs [82].

3. Shape of the KER distribution of 2D⁺ + D and D⁺ + D₂⁺ pathways

As shown in Fig. 8, the peak for the 2D⁺ + D pathway is much broader than that of the D⁺ + D₂⁺ pathway, and the same tendency was also found in experiment [7]. In order to identify the origin of the difference in the peak profiles of the two single-ionization pathways, the distributions of the total energy of the electron that ends up being bound are calculated for these two pathways and are shown in Fig. 10. These distributions are constructed as a histogram by inspecting all trajectories leading to the final state, and counting the number of trajectories with electrons having energy in a particular energy bin at a particular instant of time. The distributions are shown at four different times; three during the pulse and one shortly after the pulse. In the first panel [Fig. 10(a)], at the onset of the laser pulse, the distributions of the two pathways are similar, showing that the final state could not be predicted only from the initial energy distribution. As shown in Figs. 10(b) and 10(c), the shapes of the two distributions vary as a function of time by being driven by the pulsed laser field. For the 2D⁺ + D pathway, a small part of the population seen in Figs. 10(b) and 10(c) has positive energy, $\varepsilon_{\text{bound}}^{(e)} > 0$, indicating that an electron is ejected from the D atom. These electrons later return to the deuteron to form a D atom and can be seen in Fig. 10(d) as the small peak at small negative energy $\varepsilon_{\text{bound}}^{(e)} \approx -0.1$. This part of the population representing an electron that is first ejected

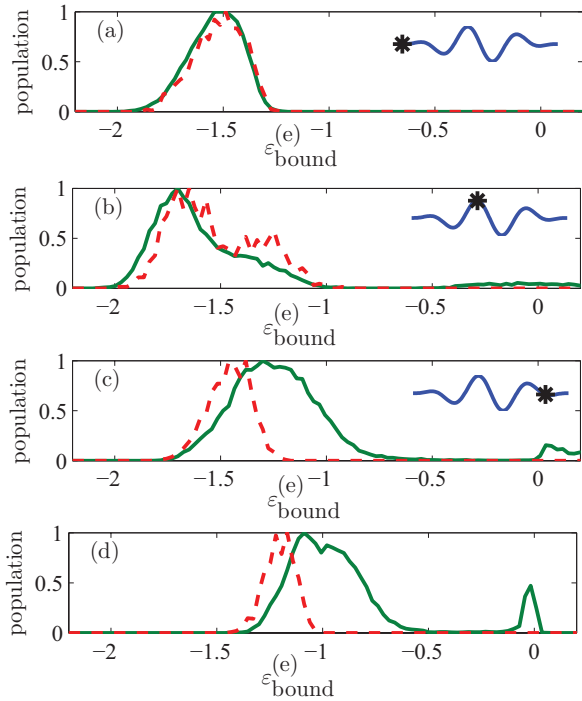


FIG. 10. (Color online) Normalized distribution of single-particle energy [measured in a.u.; see Eq. (12) for the definition] of electron that is bound in final state. The laser intensity is the same as in Fig. 8: 4×10^{15} W/cm². The solid line refers to the $2D^+ + D$ pathway and the dashed line to the $D^+ + D_2^+$ pathway. In panels (a), (b), and (c), the electric field of the laser pulse (in arbitrary units) is shown in the inset, with the time instant of the panel indicated with an asterisk. The distribution in (d) occurs 52 a.u. of time after the laser pulse has passed. The total duration of the laser pulse is $T = 327$.

and later recombines to become bound is the reason for the high-energy peak of the $2D^+ + D$ pathway, as discussed in Sec. IV C 2.

The kinetic energy distributions of the bound electron in D and D_2^+ in Fig. 10 are remarkably similar to the KER distributions of the $2D^+ + D$ and $D^+ + D_2^+$ pathways in Fig. 8(a), showing that the two kinds of distributions are related with each other. In order to explain this point more clearly, we first note that a bound electron reduces the repulsion between the deuterons by the shielding. If the bound electron is excited, it provides less shielding than a less-excited electron. When the extent of the shielding is less, the repulsive force between the shielded deuteron and another deuteron becomes larger and, consequently, the kinetic energies of the final fragments become higher. Therefore, if the bound electron is excited, as can be seen in Fig. 10 for the $2D^+ + D$ pathway, the resulting KER becomes comparatively high. On the other hand, the D_2^+ molecule could not remain bound if the electron in D_2^+ is highly excited, as described in more detail below. Therefore, only a rather narrow interval of energies of the bound electron can lead to the $D^+ + D_2^+$ pathway, resulting in the narrow KER peak of this pathway. As can be seen in Fig. 10(d), the lower limits of the energy of the bound electron are the same for the $2D^+ + D$ and $D^+ + D_2^+$ pathways. This lower-limit energy represents the energy of an electron in the ground state of D_3^{2+} .

In order to investigate the characteristics of the bound states of D_2^+ in the model, a small amount of momentum is added to an electron in D_2^+ in the equilibrium configuration, and the equations of motion are solved without the laser field for examining whether D_2^+ dissociates or stays bound. By repeating this procedure with many different initial conditions of different momenta and total energies, it was found that, (i) when the total energy ϵ_{tot} is below the ground-state energy of D, $\epsilon_{\text{tot}} < -0.5$, the dissociation does not occur, representing that our model D_2^+ supports bound and excited trajectories in the energy range of $\epsilon_0(D_2^+) < \epsilon_{\text{tot}} < -0.5$, where $\epsilon_0(D_2^+) = -0.6$ is the ground-state energy of D_2^+ ; (ii) when the total energy is $-0.5 < \epsilon_{\text{tot}} < -0.4$, there are both bound and unbound trajectories, showing that D_2^+ dissociates or does not dissociate depending on the initial momentum of the electron; (iii) when $-0.4 < \epsilon_{\text{tot}} < 1/R_e(D_2^+) = 0.43$ with $R_e(D_2^+) = 2.3$, the equilibrium distance of D_2^+ in the model, all trajectories lead to dissociation; and (iv) when $\epsilon_{\text{tot}} > 1/R_e(D_2^+)$, all trajectories lead to ionization.

In quantum mechanics, electronically excited states of H_2^+ are in general unstable and dissociate promptly. The only exceptions are the two excited states, $3d\sigma_g$ and $2p\pi_u$, whose potential energy curves support bound vibrational states in the BO approximation [83,84]. The theoretical energy of these excited states measured from the $1s\sigma_g$ ground state of H_2^+ at the equilibrium internuclear distance $R_e = 2.0$ are $\epsilon_{2p\pi_u}(R_e) - \epsilon_{1s\sigma_g}(R_e) = 0.67$ and $\epsilon_{3d\sigma_g}(R_e) - \epsilon_{1s\sigma_g}(R_e) = 0.87$ [84].

4. KER spectra at low field intensity

At the intensity of 1.4×10^{15} W/cm², the yields of all the seven pathways are sufficiently large, and their KER distributions are obtained with relatively small uncertainties. The KER histograms at 1.4×10^{15} W/cm² are shown in Fig. 11 for both D_3^+ and H_3^+ . The energy positions of the peaks for the ionization pathways are shifted slightly by ~ 0.1 towards the lower-energy side compared to the corresponding peaks in Fig. 8 obtained when the laser intensity is 4×10^{15} W/cm². The peaks for the nonionizing $D_2^+ + D$ and $D^+ + D_2$ pathways are seen in the very low KER region. It can also be seen in Fig. 11 that the peak position in the KER distribution at $\text{KER} \sim 0.4$ for the $D^+ + D_2$ dissociation pathway is almost the same as that of the single ionization $D^+ + D_2^+$ pathway. This can be explained also by the recombination model introduced in IV C 2 for the high-energy peak of the $2D^+ + D$ pathway; that is, one electron first escapes, and then recombines to form a D_2 molecule in which one of the two electrons is excited.

V. SUMMARY AND CONCLUSIONS

The overall purpose of this study is twofold:

The first aim is to find a practical model of laser-molecule interactions in which both nuclear motion and electronic motion in polyatomic molecules are treated in three dimensions. We have confirmed that the quasiclassical model introduced in this study fulfills this requirement.

The second aim is to answer the question ‘‘Can we investigate and discuss intense laser-molecule interaction in terms of classical mechanics?’’ We believe that we have

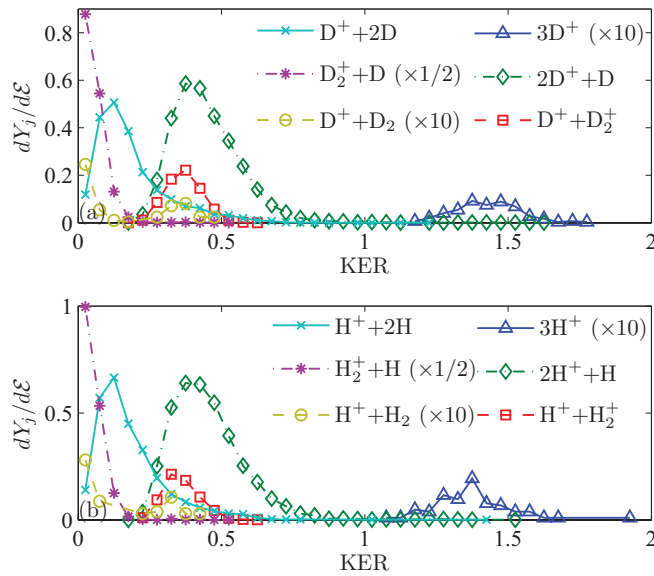


FIG. 11. (Color online) Kinetic energy release (in a.u.) for all pathways, at intensity 1.4×10^{15} W/cm², for (a) D₃⁺ and (b) H₃⁺. Each point corresponds to an energy bin, and only bins with nonzero counts are shown. The statistical error bars are of the same size or smaller than the curve symbols. Note in both panels the curves for the D⁺ + D₂ (H⁺ + H₂) and 3D⁺ (3H⁺) pathways have been multiplied by a factor of 10 and by a factor of 1/2 for the D₂⁺ + D (H₂⁺ + H) pathways.

answered this question in the affirmative. As a demonstration of the usefulness of the model, we have shown that both KER and angular distributions measured in the previous experiments are qualitatively reproduced by the simulation.

Classical simulations of laser-molecule interactions have many advantages over quantum calculations. There is no need to restrict the dimensions of the model or the number of active electrons in solving the classical equations of motion, contrary to the situation in which we solve numerically the time-dependent Schrödinger equation. Furthermore, in classical calculations, large-amplitude motion of the electrons in the oscillating electric field of the laser is treated without any difficulties. This enabled us to find the interesting high-energy channel of the D₃⁺ → D⁺ + D⁺ + D process, which probably could not have been noticed with a quantum method employing a finite-size grid for the wave-function propagation.

One important finding in the present investigation is that intramolecular dynamics of the excited electrons within D₃⁺ can also be adequately treated as demonstrated in Sec. IV C3. We have thus shown that all processes pertinent to laser-molecule interaction, ionization, dissociation, and excitation can be consistently treated within the present theoretical framework. As for the extension of the model, we will be able to treat larger molecules with the same kind of auxiliary, quasiclassical potentials. If sufficient care is taken to reproduce the essential features of the ground-state PES, we should be able to deepen our understanding of the complex laser-induced classical motion of electrons and protons in larger polyatomic molecules.

Of course, we should point out the inherent shortcomings of a classical model. Intrinsic quantum effects such as tunneling and interference could not be treated in the model. Thus,

if such effects are important in understanding experimental results, the model will inevitably fail. Therefore, we could not use the present model when tunneling is the dominant ionization mechanism. In our calculations in Sec. III, we have found significant ionization which proceeds through the over-the-barrier mechanism when the laser field intensity is larger than 10¹⁵ W/cm², but we could not judge from classical calculations alone if interference is important or not in this over-the-barrier ionization. It will therefore be interesting to compare the present quasiclassical calculations with quantum calculations, if such quantum results become available in the future. A possible sign of a failure due to the omission of the interference is the inability to reproduce the experimental patterns in the χ distributions appearing in Fig. 5 in Sec. IV B. If a particular spectrum or distribution cannot be reproduced with the classical model, we can say that the mechanism should have a quantum origin.

ACKNOWLEDGMENTS

This work was supported by the Ministry of Education, Culture, Sports, Science and Technology (MEXT), Japan (Grant-in-Aid for Specially Promoted Research on Ultrafast Hydrogen Migration No. 19002006 and Grant-in-Aid for Global COE Program for Chemistry Innovation). E. L. acknowledges a Grant-in-Aid for Scientific Research (No. 21-09238) from the Japan Society for the Promotion of Science (JSPS).

APPENDIX A: INITIAL CONDITIONS

Initial conditions are calculated in the following way. From the equilibrium configuration (with total energy $\epsilon_0 = -1.34$), the three nuclei are displaced by a small distance in random directions and subsequently the positions and momenta of the electrons are optimized to minimize the total energy in the new nuclear configuration. If the total energy satisfies $0.06 \leq \epsilon_{\text{tot}} - \epsilon_0 \leq 0.1$, the new configuration is chosen as a starting configuration, otherwise the random displacement of the nuclei is repeated. This addition of the small amount of energy into the system is considered to be vibrational excitation prepared in the initial state. After the injection of vibrational energy into the molecule, it is no longer in its vibrational ground state. From the starting configuration obtained as described above, a trajectory is calculated by making the system evolve without influence of the laser field. Positions and momenta of the particles on the resulting trajectory at different instants in time are then used as initial values for the subsequent runs with the laser field present. Such a single field-free trajectory is used for 100 runs with the laser field. This means that the total energy of these 100 runs at the beginning is the same, but that the relative positions and momenta of the particles differ. Before each run, the molecule is randomly rotated in the following way: First, two sets of three rotation angles are randomly chosen. One of these sets are then used to rotate all the position vectors, and the other set to rotate all momentum vectors. Recall that the total Hamiltonian (6) is invariant under overall rotations of both the positions and the momenta, separately, so that an overall rotation will not change the total energy. The initial rotation is made to prepare an ensemble of randomly oriented molecules. We adopted this procedure to simulate the typical experimental

situation where an ensemble of randomly oriented molecules in the gas phase is used.

APPENDIX B: NUMERICAL ERRORS IN CALCULATIONS

The numerical errors in the solution of the equations of motion (7) are monitored by checking the identity

$$H_{D_3^+}(t) = \int_0^t \mathbf{E}(\tau) \cdot \left[\sum_{j=1}^3 \frac{d\mathbf{R}_j}{dt}(\tau) - \sum_{k=1}^2 \frac{d\mathbf{r}_k}{dt}(\tau) \right] d\tau + H_{D_3^+}(0). \quad (\text{B1})$$

It was confirmed that, when the code is run without the external field, the total energy is conserved to within a relative error of $e_{\text{rel}} = 10^{-6}$, where the relative error is defined as

$$e_{\text{rel}} = \frac{1}{|H_{D_3^+}(t)|} \left| \int_0^t \mathbf{E}(\tau) \cdot \left[\sum_{j=1}^3 \frac{d\mathbf{R}_j}{dt}(\tau) - \sum_{k=1}^2 \frac{d\mathbf{r}_k}{dt}(\tau) \right] d\tau + H_{D_3^+}(0) - H_{D_3^+}(t) \right|. \quad (\text{B2})$$

When the intense laser field was introduced, it was confirmed that Eq. (B1) is satisfied within a relative error of $e_{\text{rel}} = 10^{-5}$ throughout the calculations in the present study.

-
- [1] F. Krausz and M. Ivanov, *Rev. Mod. Phys.* **81**, 163 (2009).
- [2] K. Sändig, H. Figger, and T. W. Hänsch, *Phys. Rev. Lett.* **85**, 4876 (2000).
- [3] F. Kelkensberg, C. Lefebvre, W. Siu, O. Ghafur, T. T. Nguyen-Dang, O. Atabek, A. Keller, V. Serov, P. Johnsson, M. Swoboda, T. Remetter, A. LHuillier, S. Zherebtsov, G. Sansone, E. Benedetti, F. Ferrari, M. Nisoli, F. Lepine, M. F. Kling, and M. J. J. Vrakking, *Phys. Rev. Lett.* **103**, 123005 (2009).
- [4] V. S. Prabhudesai, U. Lev, A. Natan, B. D. Bruner, A. Diner, O. Heber, D. Strasser, D. Schwalm, I. Ben-Itzhak, J. J. Hua, B. D. Esry, Y. Silberberg, and D. Zafman, *Phys. Rev. A* **81**, 023401 (2010).
- [5] A. Staudte, D. Pavičić, S. Chelkowski, D. Zeidler, M. Meckel, H. Niikura, M. Schöffler, S. Schössler, B. Ulrich, P. P. Rajeev, T. Weber, T. Jahnke, D. M. Villeneuve, A. D. Bandrauk, C. L. Cocke, P. B. Corkum, and R. Dörner, *Phys. Rev. Lett.* **98**, 073003 (2007).
- [6] A. Staudte, S. Patchkovskii, D. Pavičić, H. Akagi, O. Smirnova, D. Zeidler, M. Meckel, D. M. Villeneuve, R. Dörner, M. Y. Ivanov, and P. B. Corkum, *Phys. Rev. Lett.* **102**, 033004 (2009).
- [7] J. McKenna, A. M. Sayler, B. Gaire, N. G. Johnson, K. D. Carnes, B. D. Esry, and I. Ben-Itzhak, *Phys. Rev. Lett.* **103**, 103004 (2009).
- [8] J. D. Alexander, C. R. Calvert, R. B. King, O. Kelly, L. Graham, W. A. Bryan, G. R. A. J. Nemeth, W. R. Newell, C. A. Froud, I. C. E. Turcu, E. Springate, I. D. Williams, and J. B. Greenwood, *J. Phys. B* **42**, 141004 (2009).
- [9] B. Gaire, J. McKenna, M. Zohrabi, K. D. Carnes, B. D. Esry, and I. Ben-Itzhak, *Phys. Rev. A* **85**, 023419 (2012).
- [10] T. Okino, Y. Furukawa, P. Liu, T. Ichikawa, R. Itakura, K. Hoshina, K. Yamanouchi, and H. Nakano, *Chem. Phys. Lett.* **423**, 220 (2006).
- [11] A. Hishikawa, A. Matsuda, M. Fushitani, and E. J. Takahashi, *Phys. Rev. Lett.* **99**, 258302 (2007).
- [12] H. Xu, T. Okino, and K. Yamanouchi, *J. Chem. Phys.* **131**, 151102 (2009).
- [13] P. M. Kraus, M. C. Schwarzer, N. Schirmel, G. Urbasch, G. Frenking, and K.-M. Weitzel, *J. Chem. Phys.* **134**, 114302 (2011).
- [14] Y. V. Vanne and A. Saenz, *Phys. Rev. A* **80**, 053422 (2009).
- [15] S. Sukiasyan, C. McDonald, C. Van Vlack, C. Destefani, C. Varin, M. Ivanov, and T. Brabec, *Chem. Phys.* **366**, 37 (2009).
- [16] M. Awasthi, Y. V. Vanne, A. Saenz, A. Castro, and P. Decleva, *Phys. Rev. A* **77**, 063403 (2008).
- [17] M. Abu-samha and L. B. Madsen, *Phys. Rev. A* **80**, 023401 (2009).
- [18] S. Petretti, Y. V. Vanne, A. Saenz, A. Castro, and P. Decleva, *Phys. Rev. Lett.* **104**, 223001 (2010).
- [19] S. Chelkowski, T. Zuo, O. Atabek, and A. D. Bandrauk, *Phys. Rev. A* **52**, 2977 (1995).
- [20] I. Kawata, H. Kono, and Y. Fujimura, *Chem. Phys. Lett.* **289**, 546 (1998).
- [21] S. Pieper and M. Lein, *Phys. Rev. A* **77**, 041403 (2008).
- [22] F. Anis, T. Cackowski, and B. D. Esry, *J. Phys. B* **42**, 091001 (2009).
- [23] A. Kästner, F. Grossmann, R. Schmidt, and J.-M. Rost, *Phys. Rev. A* **81**, 023414 (2010).
- [24] M. Ma, E. Suraud, and P.-G. Reinhard, *Eur. Phys. J. D* **14**, 217 (2001).
- [25] B. Rotenberg, R. Taïeb, V. Véniard, and A. Maquet, *J. Phys. B* **35**, L397 (2002).
- [26] M. Uhlmann, T. Kunert, F. Grossmann, and R. Schmidt, *Phys. Rev. A* **67**, 013413 (2003).
- [27] M. Ma, P.-G. Reinhard, and E. Suraud, *Eur. Phys. J. D* **33**, 49 (2005).
- [28] C. Ruiz, L. Plaja, R. Taïieb, V. Véniard, and A. Maquet, *Phys. Rev. A* **73**, 063411 (2006).
- [29] M. Isla and J. A. Alonso, *J. Phys. Chem. C* **111**, 17765 (2007).
- [30] G. Camiolo, G. Castiglia, P. P. Corso, E. Fiordilino, and J. P. Marangos, *Phys. Rev. A* **79**, 063401 (2009).
- [31] H. A. Leth, L. B. Madsen, and K. Mølmer, *Phys. Rev. Lett.* **103**, 183601 (2009).
- [32] H. A. Leth, L. B. Madsen, and K. Mølmer, *Phys. Rev. A* **81**, 053409 (2010).
- [33] T. Kato and K. Yamanouchi, *J. Chem. Phys.* **131**, 164118 (2009).
- [34] M. Nest, *Chem. Phys. Lett.* **472**, 171 (2009).
- [35] C. Jhala and M. Lein, *Phys. Rev. A* **81**, 063421 (2010).
- [36] J. G. Leopold and I. C. Percival, *Phys. Rev. Lett.* **41**, 944 (1978).
- [37] J. A. Griffiths and D. Farrelly, *Phys. Rev. A* **45**, R2678 (1992).
- [38] D. Bauer, *Phys. Rev. A* **56**, 3028 (1997).

- [39] P. B. Lerner, K. J. LaGattuta, and J. S. Cohen, *Phys. Rev. A* **49**, R12 (1994).
- [40] K. J. LaGattuta and J. S. Cohen, *J. Phys. B* **31**, 5281 (1998).
- [41] R. Panfili, S. L. Haan, and J. H. Eberly, *Phys. Rev. Lett.* **89**, 113001 (2002).
- [42] P. J. Ho, R. Panfili, S. L. Haan, and J. H. Eberly, *Phys. Rev. Lett.* **94**, 093002 (2005).
- [43] K. N. Shomsky, Z. S. Smith, and S. L. Haan, *Phys. Rev. A* **79**, 061402 (2009).
- [44] T. Fennel, L. Ramunno, and T. Brabec, *Phys. Rev. Lett.* **99**, 233401 (2007).
- [45] M. Kundu and D. Bauer, *Phys. Plasmas* **15**, 033303 (2008).
- [46] T. Fennel, K.-H. Meiwes-Broer, J. Tiggesbäumker, P.-G. Reinhard, P. M. Dinh, and E. Suraud, *Rev. Mod. Phys.* **82**, 1793 (2010).
- [47] P. J. Ho and J. H. Eberly, *Phys. Rev. Lett.* **97**, 083001 (2006).
- [48] F. Mauger, C. Chandre, and T. Uzer, *Phys. Rev. Lett.* **104**, 043005 (2010).
- [49] D. M. Villeneuve, M. Y. Ivanov, and P. B. Corkum, *Phys. Rev. A* **54**, 736 (1996).
- [50] L. Wilets, E. Henley, M. Kraft, and A. Mackellar, *Nucl. Phys. A* **282**, 341 (1977).
- [51] C. L. Kirschbaum and L. Wilets, *Phys. Rev. A* **21**, 834 (1980).
- [52] J. S. Cohen, *Phys. Rev. A* **51**, 266 (1995).
- [53] J. S. Cohen, *Phys. Rev. A* **56**, 3583 (1997).
- [54] L. Wilets and J. S. Cohen, *Contemp. Phys.* **39**, 163 (1998).
- [55] J. S. Cohen, *Phys. Rev. A* **57**, 4964 (1998).
- [56] J. S. Cohen, *Phys. Rev. A* **59**, 4300 (1999).
- [57] J. S. Cohen, *Phys. Rev. A* **59**, 1160 (1999).
- [58] J. S. Cohen, *J. Phys. B* **38**, 441 (2005).
- [59] J. S. Cohen, *J. Phys. B* **39**, 3561 (2006).
- [60] J. S. Cohen, *J. Phys. B* **39**, 1517 (2006).
- [61] D. A. Wasson and S. E. Koonin, *Phys. Rev. A* **39**, 5676 (1989).
- [62] P. B. Lerner, K. LaGattuta, and J. S. Cohen, *Laser Phys.* **3**, 331 (1993).
- [63] K. J. LaGattuta, *Phys. Rev. A* **73**, 043404 (2006).
- [64] A. D. Bandrauk and H. Yu, *Phys. Rev. A* **59**, 539 (1999).
- [65] I. Kawata, H. Kono, and A. D. Bandrauk, *Phys. Rev. A* **64**, 043411 (2001).
- [66] E. Lötstedt, T. Kato, and K. Yamanouchi, *Phys. Rev. Lett.* **106**, 203001 (2011).
- [67] D. S. Tchitchekova, H. Lu, S. Chelkowski, and A. D. Bandrauk, *J. Phys. B* **44**, 065601 (2011).
- [68] C. S. Jones and M. S. Murrillo, *High Ener. Dens. Phys.* **3**, 379 (2007).
- [69] D. Frye, A. Preiskorn, G. C. Lie, and E. Clementi, *J. Chem. Phys.* **92**, 4948 (1990).
- [70] W. H. Press, S. A. Teukolsky, W. T. Vetterling, and B. P. Flannery, *Numerical Recipes in Fortran 77: The Art of Scientific Computing* (Cambridge University Press, Cambridge, 1992).
- [71] W. Kolos and L. Wolniewicz, *J. Phys. Chem.* **43**, 2429 (1965).
- [72] M. M. Madsen and J. M. Peek, *At. Data* **2**, 171 (1970).
- [73] M. W. Schmidt, K. K. Baldrige, J. A. Boatz, S. T. Elbert, M. S. Gordon, J. H. Jensen, S. Koseki, N. Matsunaga, K. A. Nguyen, S. Su, T. L. Windus, M. Dupuis, and J. A. Montgomery Jr., *J. Comput. Chem.* **14**, 1347 (1993).
- [74] C. L. Pekeris, *Phys. Rev.* **126**, 1470 (1962).
- [75] P. Wang, A. M. Saylor, K. D. Carnes, B. D. Esry, and I. Ben-Itzhak, *Opt. Lett.* **30**, 664 (2005).
- [76] J. H. Posthumus, *Rep. Prog. Phys.* **67**, 623 (2004).
- [77] K. Ishikawa and T. Blenski, *Phys. Rev. A* **61**, 063408 (2000).
- [78] B. Manschwetus, T. Nubbemeyer, K. Gorling, G. Steinmeyer, U. Eichmann, H. Rottke, and W. Sandner, *Phys. Rev. Lett.* **102**, 113002 (2009).
- [79] A. Emmanouilidou, C. Lazarou, A. Staudte, and U. Eichmann, *Phys. Rev. A* **85**, 011402(R) (2012).
- [80] J. McKenna, S. Zeng, J. J. Hua, A. M. Saylor, M. Zohrabi, N. G. Johnson, B. Gaire, K. D. Carnes, B. D. Esry, and I. Ben-Itzhak, *Phys. Rev. A* **84**, 043425 (2011).
- [81] F. A. Ilkov, J. E. Decker, and S. L. Chin, *J. Phys. B* **25**, 4005 (1992).
- [82] J. McKenna *et al.* (private communication).
- [83] G. H. Dunn, R. Geballe, and D. Pretzer, *Phys. Rev.* **128**, 2200 (1962).
- [84] T. E. Sharp, *At. Data* **2**, 119 (1971).